analytical chemistry

pubs.acs.org/ac Article

Chemiluminescence-Derived Self-Powered Photoelectrochemical Immunoassay for Detecting a Low-Abundance Disease-Related Protein

Zhichao Yu, Hexiang Gong, Yuxuan Li, Jianhui Xu, Jin Zhang, Yongyi Zeng, Xiaolong Liu, and Dianping Tang*

Cite This: *Anal. Chem.* 2021, 93, 13389−13397 Read Online

ACCESS | Metrics & More | Article Recommendations | Supporting Information

ABSTRACT: Early diagnosis of cancers relies on the sensitive detection of specific biomarkers, but most of the current testing methods are inaccessible to home healthcare due to cumbersome steps, prolonged testing time, and utilization of toxic and hazardous substances. Herein, we developed a portable self-powered photoelectrochemical (PEC) sensing platform for rapid detection of prostate-specific antigen (PSA, as a model disease-related protein) by integrating a self-powered photoelectric signal output system catalyzed with chemiluminescence-functionalized Au nanoparticles (AuNPs) and a phosphomolybdic acid (PMA)-based photochromic visualization platform. TiO_2-g-C_3N_4-PMA photosensitive materials were first synthesized and functionalized on a sensor chip. The sensor consisted of filter paper modified with a photocatalytic material and a regional laser-etched FTO electrode as an alternative to a conventional PEC sensor with a glass-based electrode. The targeting system involved a monoclonal anti-PSA capture antibody-functionalized Fe_3O_4 magnetic bead (mAb_1-MB) and a polyclonal anti-PSA antibody (pAb_2)-*N*-(4-aminobutyl)-*N*-ethylisoluminol-AuNP (ABEI-AuNP). Based on the signal intensity of the chemiluminescent system, the photochromic device color changed from light yellow to heteropoly blue through the PMA photoelectric materials integrated into the electrode for visualization of the signal output. In addition, the electrical signal in the PEC system was amplified by a sandwich-type capacitor and readout on a handheld digital multimeter. Under optimum conditions, the sensor exhibited high sensitivity relative to PSA in the range of 0.01−50 ng mL^{-1} with a low detection limit of 6.25 pg mL^{-1}. The flow-through chemiluminescence reactor with a semiautomatic injection device and magnetic separation was avoid of unstable light source intensity inherent in the chemiluminescence process. Therefore, our strategy provides a new horizon for point-of-care analysis and rapid cost-effective clinical diagnosis.

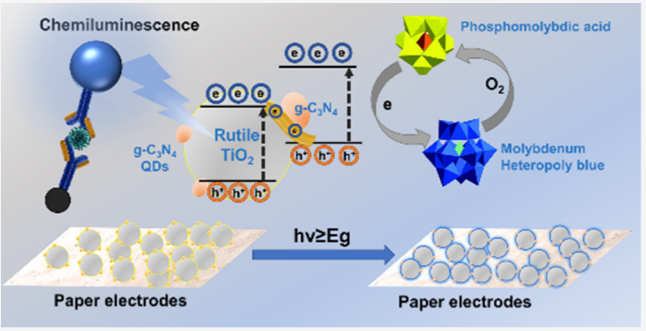

With the fast-growing demand for point-of-care tests (POCTs) and rapid assays, paper-based devices, including microfluidic paper-based analytical devices (μPADs) and paper electrodes (PEs), have gained the attention of researchers due to their manageable cost, ease of manufacture, portability, and maneuverability.[1−8] Attracted by the advantages of paper-based applications, many communities are striving to develop innovative and pragmatic test platforms to satisfy the testing concerns in resource-limited and developing countries, including the development of paper-based coupled colorimetric,[9−11] (photo)electrochemical,[12−15] chemiluminescent,[16,17] and fluorescence testing methods.[18−20]

Photoelectrochemical (PEC) biomonitoring assays, a kind of popular research hot spots, have become popular among research scholars due to their easy operation and high sensitivity. As the core device of the PEC biosensors, the signal converter, typically consisting of an electrode of photoelectric material, outputs electrical signals affected by the target under light conditions.[21−24] The construction of the PEC sensing platform, however, relies on electrochemical workstations and physical light sources, making the monitoring device complex and valuable, which limits the application scenarios of PEC assays. Intriguingly, recent studies have shown that self-powered chemiluminescence (SP-CL) can replace physical light sources to excite the electron and hole separation of photo-active substances, thus contributing to the portability and miniaturization of detection devices.[25−27] Owing to the high sensitivity, low cost, and portable design

Received: August 6, 2021
Accepted: September 13, 2021
Published: September 23, 2021

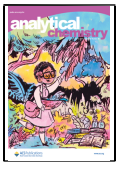

https://doi.org/10.1021/acs.analchem.1c03344
Anal. Chem. 2021, 93, 13389−13397

Scheme 1. Schematic Diagram of the PE and the Paper-Based Supercapacitor and the DMM Readout of the PEC Immunoassay Model for PSA Detection by the Sandwich Immunoassay Model Triggered by Magnetic Bead Separation with an ABEI Self-Powered Supply System Coupled to the TiO_2-g-C_3N_4-PMA Photosensitive Material (mAb_1: Monoclonal Anti-PSA Capture Antibody; pAb_2: Polyclonal Anti-PSA Detection Antibody; and AuNP: Gold Nanoparticle)

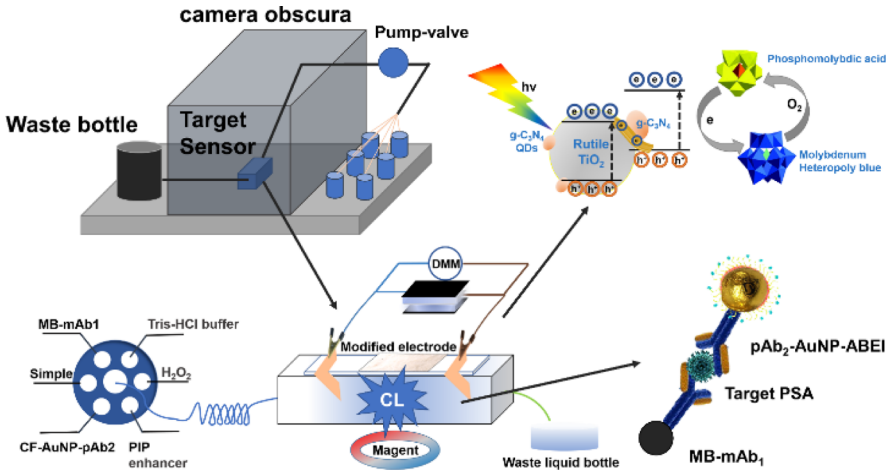

of the PEC-CL biological platform, the chemiluminescence-based PEC sensing platform is considered to have great potential for POCTs and home health management and to be further developed and investigated in the future.

A critical factor to consider in constructing new self-powered photoelectrochemical (SP-PEC) biosensors is the exploitation of high-performance photosensitive materials. As a semiconductor with good chemical stability and suitable energy band structure, TiO_2 has been demonstrated to be a promising photoanode material and used in photocatalysis and photoelectrochemistry.[28,29] Nevertheless, the inherent wide band gap of TiO_2 limits its utilization of visible light. Currently, strategies that have proven to be concentrated include dyes, quantum dots (QDs), up-conversion materials, and heterojunction sensitization TiO_2.[29−32] Li *et al.* constructed TiO_2 nanospheres modified by g-C_3N_4 quantum dots (CN QDs), which improved the ability to capture visible light and delayed the recombination of photogenerated electron−hole pairs.[33] Therefore, the development of TiO_2 heterostructures is imperative as a candidate for visible light absorption-driven PEC.

Attractively, polyoxometalates (POMs) are a class of metal clusters with good multielectron redox characteristics and uniform size less than 1.0 nm, which are widely used in catalysis, solar cells, and biomedicine.[34,35] Phosphomolybdic acid (PMA), a typical representative of POM family, shows a classical Keggin configuration and has been proved to be a processable *p*-type dopant.[36−38] The construction of a heterojunction between a semiconductor and POM can effectively combine the photoelectronic properties of the semiconductor with the unique electrochemically active behavior of POM.[39,40] However, to the best of our knowledge, studies that independently applied the electro-redox properties of PMA predominate upon our review.[41−44] Logically, due to the redox characteristics of PMA, under the condition of optical excitation, it is completely conditional to act as a sacrificial agent for the separation of electrons and holes. Therefore, there will be expected advantages in constructing a PMA-type heterostructure.

Herein, we report a chemiluminescence-powered automated PEC immunosensing platform based on PE and paper capacitor amplification for rapid detection of cancer markers, with prostate-specific antigen (PSA) as a proof of concept. To the best of our knowledge, it is the first PEC sensing platform based on PE and chemiluminescence support to detect cancer markers. The entire testing process can be completed within 35 min without the hassle of bulky PEC test sets, and the cost is affordable in most home and POCT environments. Scheme 1 shows the detection principle of the platform and the related construction. The platform integrates the chemiluminescence system with *p*-iodophenol (PIP) as the enhancer and the filter paper loaded with photoelectric materials as a photoelectric convertor and designs the portable and automatic integration of the sampling system. In short, we first synthesize the TiO_2-g-C_3N_4-PMA heterostructure by a simple hydrothermal method and verify its photoelectric and photochromic properties. Suitable doping of g-C_3N_4 enables the wavelength of ABEI-based chemiluminescence to be catered for, and the construction of Z-scheme heterojunction can effectively transfer photogenerated carriers. For the detection of a biological target, the target is recognized by the captured antibody and forms a bead-based sandwich-type immune complex with an ABEI-Au-labeled detection antibody and then is separated by an external magnet. Due to the inherent redox characteristics of the TiO_2-g-C_3N_4-PMA outer layer of the core−shell structure, the paper-based loaded heterojunction changes color with the change of PSA dose, thus serving as a visual window. The paper-based capacitor acts as a charge memory and monitors the photocurrent over a period of time (40 s). After shorting the capacitor, the digital multimeter (DMM) reading is used as the basis for quantifying the PSA concentration, and the photochromic window can be used for rapid diagnosis of clinical diseases. This work provides a flexible PE PEC test platform with automatic sample introduction without external light sources and is expected to be used for accurate and semiquantitative testing in different scenarios.

EXPERIMENTAL SECTION

Synthesis of TiO_2-g-C_3N_4 Heterojunction and TiO_2-g-C_3N_4-PMA Core−Shell Structure. The synthesis of TiO_2-g-C_3N_4 heterojunction was based on the previous method with

https://doi.org/10.1021/acs.analchem.1c03344
Anal. Chem. 2021, 93, 13389−13397

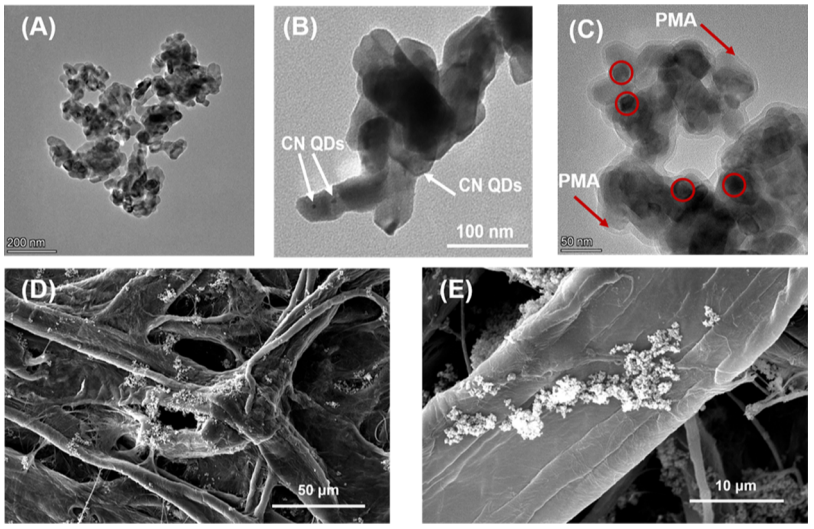

Figure 1. (A–C) TEM images of TiO_2-g-C_3N_4-PMA at different magnifications (note: The red circles represented g-C_3N_4 quantum dots and the red and white arrows indicated the presence of PMA and CN QDs) and (D,E) SEM images of TiO_2-g-C_3N_4-PMA nanocomposites loaded on paper at various magnifications.

slight modification.[33] Briefly, 2.0 g of commercial rutile TiO_2 was initially ground thoroughly, and then 78.9 mg of melamine was added. Then, the mixture was ground again until no particulate appeared. The milled powder was carefully transferred to a crucible with an Al_2O_3 lid, placed in a muffle furnace, heated to 500 °C at 2.5 °C min^{-1}, and held at 500 °C for 4 h. Finally, the completely cauterized sample was allowed to cool naturally at room temperature, and the final product was collected and stored properly.

A simple one-pot method was used to synthesize PMA-coated TiO_2-g-C_3N_4. Using TiO_2-g-C_3N_4 as the precursor, 2.0 g of the above substance was dissolved in 100 mL of ethanol solvent, and 2.0 g of PMA was added to it after complete dispersion, during which the solution changed from white to yellow. The mixing device was stirred under light-proof condition for 10 h. Finally, the fully reacted solution was transferred to a hot plate to allow complete evaporation of the solvent and to collect the material deposited at the bottom of the vessel, during which N_2 needed to be passed throughout to prevent thermal reduction of the PMA.

Preparation of the Paper-Based PEC Sensor. Simple physical stress was applied to the filter paper by cutting out a 1.0 cm^2 square. The appropriate concentration of synthetic TiO_2-g-C_3N_4 was applied dropwise on top of the cutout paper and transferred to an oven for drying. The above operation was repeated three times to promote the loading of the photoelectric material on the filter paper (note: The FTO electrode with the center square-etched area of 1.0 cm^2). After that, the square filter paper loaded with photoactive materials was placed on the etched area. To prevent poor contact or breakage, the paper-based electrode was encapsulated by copper adhesive around the edge area.

Immunoreaction Procedure and PEC Measurement. Scheme 1 describes the working principle and procedure of the PEC test platform for target PSA, and the synthesis of capture and recognition antibodies and other parts of the experimental procedure are described in the Supporting Information. The whole PEC test platform consisted of a sample introduction device constructed with an injection pump, a six-way sample introduction valve, and a group of glass bottles with an external polytetrafluoroethylene tube or 96-well microplates, a chemiluminescence reaction cell, and a DMM by combining with a capacitor. The injection was controlled by a six-way valve, and the flow rate was set at 600 μL min^{-1} through the detection chamber. In the presence of PSA, the capture antibody MB-mAb_1 and the detection antibody (dAb_2) formed a sandwich immune complex with PSA in the detection cell, and the unreacted antibody was removed by a magnetic field and an automatic sample introduction washing device. The specific test procedure is as follows: (i) 100 μL of mAb_1-MB was injected into the detection cell and concentrated near the PE by controlling the external magnetic field; (ii) 100 μL of the PSA standard sample/unknown sample and 100 μL of ABEI-AuNP-pAb_2 were injected into the reaction cell in turn to form the immune complex by controlling the injection valve; (iii) after a 30 min incubation, the detection cell was passed continuously with Tris-HCl buffer, and unbound antibody molecules were washed by magnetic separation; and (iv) the injector was switched and 100 μL of PIP (10 μM) and continuous H_2O_2 (0.25 M) were sequentially injected to initiate chemiluminescence. The charge generated by the chemiluminescence-excited PE was collected by a capacitor, and the PEC detection cell was switched (40 s). After charging, the direction of the switch was changed to form a loop with DMM, the instantaneous current stored in the capacitor could be read by DMM, and the current was used to monitor the PSA concentration. Meanwhile, the content of target PSA could also be judged by the colorimetric assay in the process.

RESULTS AND DISCUSSION

Characterization of TiO_2-g-C_3N_4-PMA-Based Photoelectric Nanomaterials. The analysis device and process of the CL-PEC immunoassay platform for target PSA are shown in Scheme 1. Due to the outstanding photocurrent response of TiO_2-g-C_3N_4-PMA, the successful synthesis of TiO_2-based composite materials is vital for the whole detection process and detection performance. Initially, the morphologies of the synthesized TiO_2-g-C_3N_4 and TiO_2-g-C_3N_4-PMA were measured by transmission electron microscopy (TEM; FEI Talo F200S, Thermo Scientific). As shown in Figure 1A, the

https://doi.org/10.1021/acs.analchem.1c03344
Anal. Chem. 2021, 93, 13389–13397

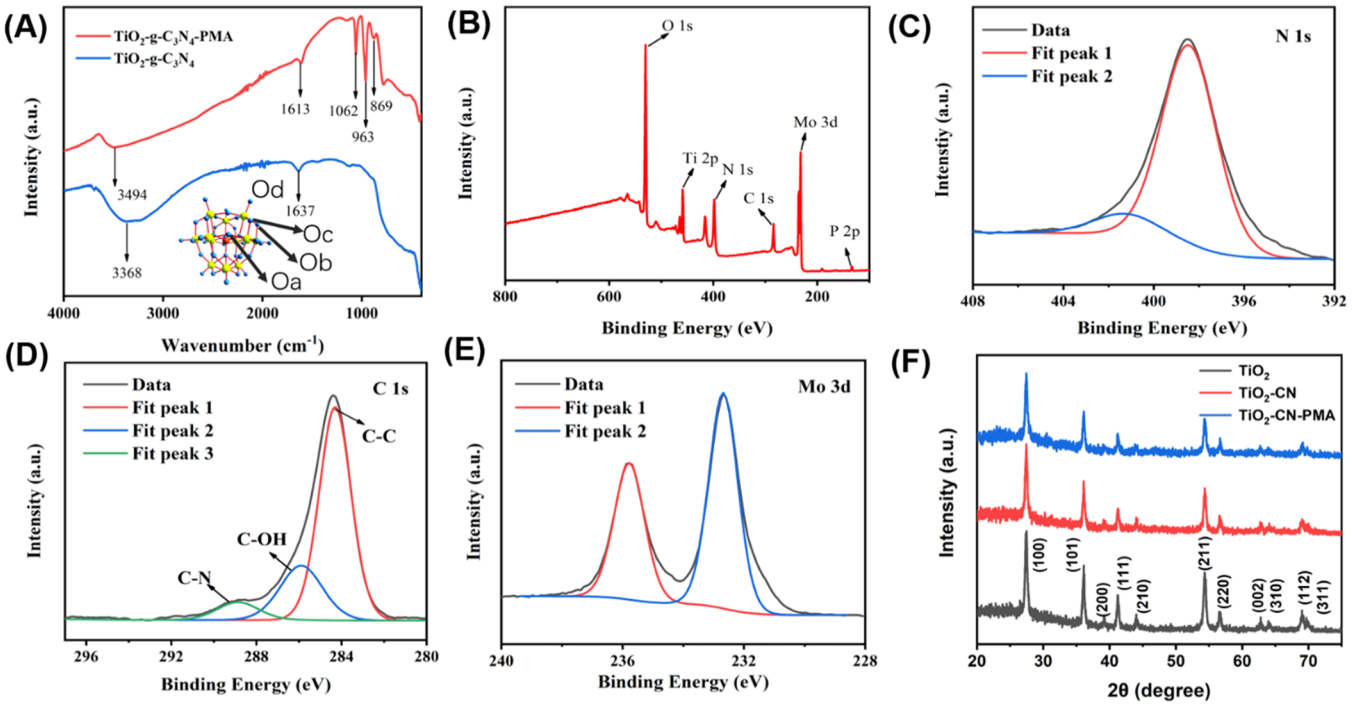

Figure 2. (A) ATR spectra of TiO_2-g-C_3N_4 before and after PMA treatment; (B) XPS patterns of composite nanomaterials; (C−E) high-resolution XPS spectra of (C) N 1s, (D) C 1s, and (E) Mo 3d; and (F) XRD patterns of TiO_2, TiO_2-CN QDs, and TiO_2-CN-PMA.

synthesized nanocomposites exhibited an amorphous shape, and there were small black particles in the amorphous material, indicating the synthesis and doping of g-C_3N_4. At a larger magnification (Figure 1B,C), it could be clearly seen that the g-C_3N_4 quantum dots were loaded on the parent TiO_2 and the PMA was uniformly encapsulated in the outer layer to form a core−shell structure. To further verify the successful synthesis of TiO_2-g-C_3N_4-PMA, we explored the change of zeta potential of the materials before and after PMA treatment. As shown in Figure S1, the zeta potentials of TiO_2 and TiO_2-g-C_3N_4 were 9.73 and 11.90 mV, respectively, which indicated that the rTiO_2 nanoparticles had a certain positive charge, and the introduction of g-C_3N_4 made the positive charge more obvious, which might be caused by some functional groups of g-C_3N_4. With the introduction of PMA, we measured a zeta potential of −39.30 mV in a neutral solution of TiO_2-g-C_3N_4-PMA, which suggested that PMA on the surface of TiO_2-g-C_3N_4-PMA played an important role in the stern layer, manifested as a transfer of the positive charge carried by the material to the negative charge. Moreover, the energy-dispersive spectrometry (EDS) pattern is shown in Figure S2, where it could be seen that the elements in the region corresponding to the TEM consist of Ti, O, C, N, Mo, and P. To determine whether the synthesized nanophotoelectric materials could be firmly loaded on the paper, we carried out scanning electron microscopy (SEM, FEI NanoSEM 50, Thermo Scientific) characterization of the nanomaterials dropped on the paper. As shown in Figure 1D,E, the spherical nanomaterial could be firmly adsorbed on the fiber of the paper, which provided the feasibility for the manufacture of the PE.

To demonstrate the structural characteristics of the synthesized composites, the attenuated total reflectance spectral (ATR; iS50, Thermo Scientific) testing results of TiO_2-g-C_3N_4 and TiO_2-g-C_3N_4-PMA are shown in Figure 2A, and the ATR spectra of g-C_3N_4 are shown in Figure S3. In the ATR spectrum of TiO_2-g-C_3N_4, two types of characteristic peaks appeared at 3494 and 1613 cm^{-1}, corresponding to the vibrations of water molecules adsorbed on the TiO_2 surface and the stretching vibration peaks of g-C_3N_4, respectively. For the TiO_2-g-C_3N_4-PMA complex structure, the ATR spectra showed additional peaks at 1062, 963, and 869 cm^{-1} as a result of PMA doping into the complex (compared with Figure S3). In detail, 1064, 963, and 869 cm^{-1} were indicated as ν(P−Oa), ν(Mo−Od), and ν(Mo−Ob−Mo), respectively, which illustrated the presence of the structure of PMA in the synthesized composite structure in the Keggin configuration (the inset of Figure 2A shows the composition of the various types of oxygen bonds in the Keggin configuration of PMA).[38] In addition, there was a 24 cm^{-1} blue shift in the C−N stretching vibration frequency in TiO_2-g-C_3N_4-PMA compared with TiO_2-g-C_3N_4, which might be mainly due to the formation of C−O−Mo bonds in the composite structure by the doping of PMA, shifting the carbon−nitrogen bonds in the carbon−nitrogen ring of g-C_3N_4 (comparison from the ATR spectrum of g-C_3N_4, Figure S3). The above results could be further demonstrated by X-ray photoelectron spectroscopy (XPS; Thermo Scientific K-Alpha). Figure 2B represents the complete XPS spectrum of the composite structure, showing the coexistence of O, Ti, N, C, Mo, and P elements, and no obvious impurities were mixed. As shown in Figure 2C, the peaks of 400.1 and 398.0 eV for N 1s could be attributed to the N atom spliced with two carbon atoms (C═N−C) and the bridging nitrogen atom N−$(C)_3$, respectively.[45] Three peaks at 284.5, 285.8, and 287.5 eV could be detected in the high-resolution spectrum of C 1s (Figure 2D), which corresponded to the C−C bonds, the tertiary carbon C−$(N)_3$ bond, and the carbon−nitrogen double bond C═N, respectively. The XPS fine spectra of C 1s and N 1s illustrated the successful loading of g-C_3N_4 in the composites. In addition, the Mo 3d spectrum

https://doi.org/10.1021/acs.analchem.1c03344
Anal. Chem. 2021, 93, 13389−13397

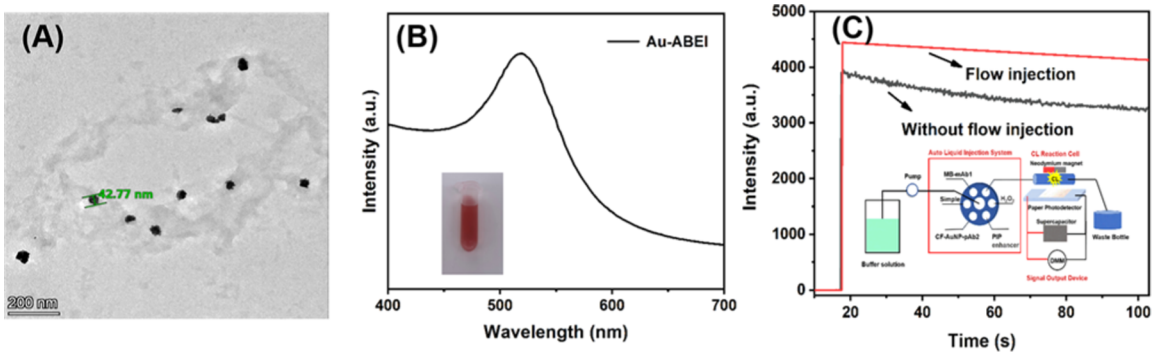

Figure 3. (A) TEM image of ABEI-AuNPs; (B) UV−vis absorption spectra of Au-ABEI; and (C) chemiluminescence intensity spectra of flow injection and direct injection at 10 mM H_2O_2.

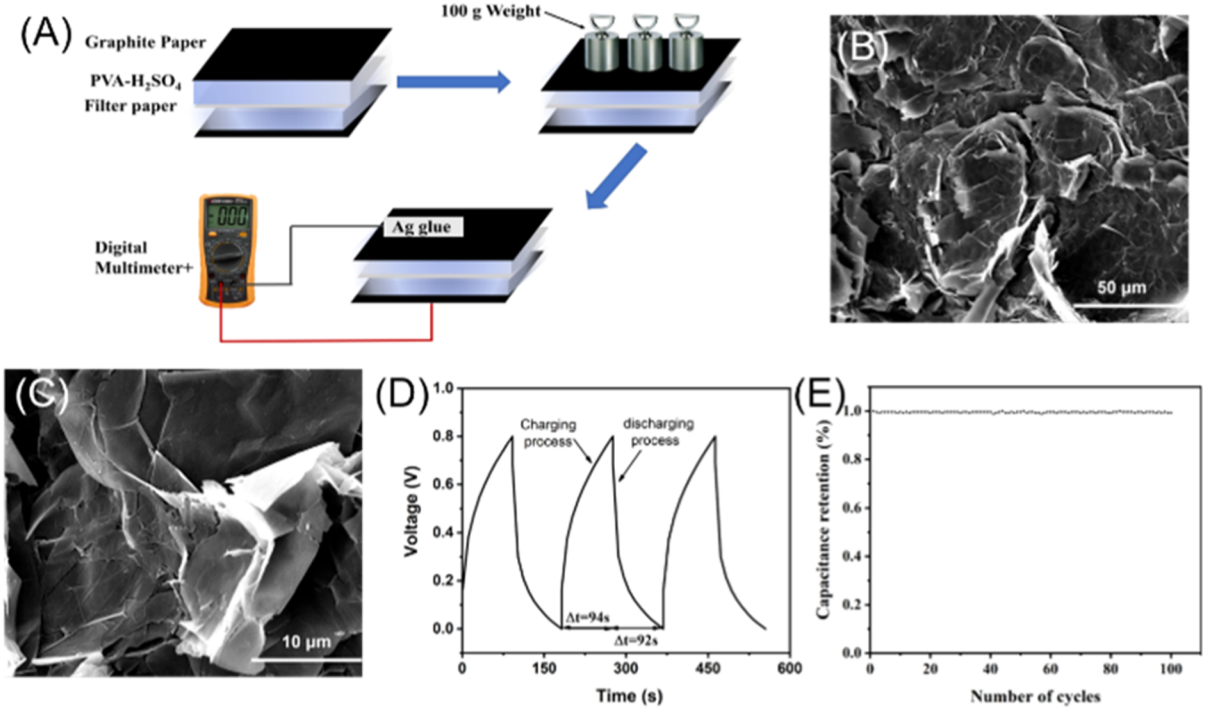

Figure 4. (A) Schematic diagram of the structure, construction, and detection method of a paper-based supercapacitor; (B) surface SEM image, and (C) SEM image under the magnification of graphite paper on the capacitor surface treated by acid; (D) galvanostatic charge−discharge curve of a paper-based supercapacitor; and (E) durability of the used capacitor under 100 charge−discharge cycles.

(Figure 2E) could be well decomposed into $3d_{5/2}$ and $3d_{7/2}$ double peaks with different spin−orbit coupling corresponding to the binding energy values of 232.9 and 235.8 eV, respectively. Combined with the results of ATR spectroscopy and related studies, the XPS high-resolution spectra of Mo demonstrated the presence of Mo−O−Ti bonds in the composites, which would facilitate the directional movement of carriers in the photoelectric process.[46] Depicted in Figure S4 is that the binding energy of Ti $2p_{1/2}$ and Ti $2p_{3/2}$ was perceived at 464.6 and 458.5 eV, respectively, which corresponded to Ti^{4+} in TiO_2 concurring to the previous results.[47] The crystallinity of the parent material rTiO_2 and the composite was confirmed by the XRD shown in Figure 2F. No other characteristic peaks of any impurity phase were observed in both the pure parent material and the composite, indicating that the synthesized material had good crystallinity. Moreover, the doping of g-C_3N_4 did not change the crystallinity of the original TiO_2, which might be due to the small amount of doped g-C_3N_4 (red line). After acidification with PMA, the crystallinity was also unchanged (blue line), indicating that introduction of PMA only loaded on the surface of the parent TiO_2, which did not change the crystallization of TiO_2−g-C_3N_4.[46] The above indicated the successful synthesis of composite photoelectric materials.

Characterization of AuNP-ABEI-Luminol System. Luminol, as a classical chemiluminescent system, can be used as an alternative light source for excitation light. Unfortunately, it is difficult to accommodate the conventional luminol system to the general PEC system due to its low luminescence efficiency. Therefore, we constructed a PIP-enhanced ABEI-AuNP-based chemiluminescence system for the amplification of the physical light source in the PEC strategy. As shown in Figure 3A, the chemiluminescence-functionalized Au nanoparticles (CF-AuNPs) synthesized exhibited a spherical structure similar to that of the cluster complex, and the chain-shaped AuNPs was around 42 nm. The UV−vis absorption spectrum of the synthesized CF-AuNPs is shown in Figure 3B. It could be seen that the synthesized

https://doi.org/10.1021/acs.analchem.1c03344
Anal. Chem. 2021, 93, 13389−13397

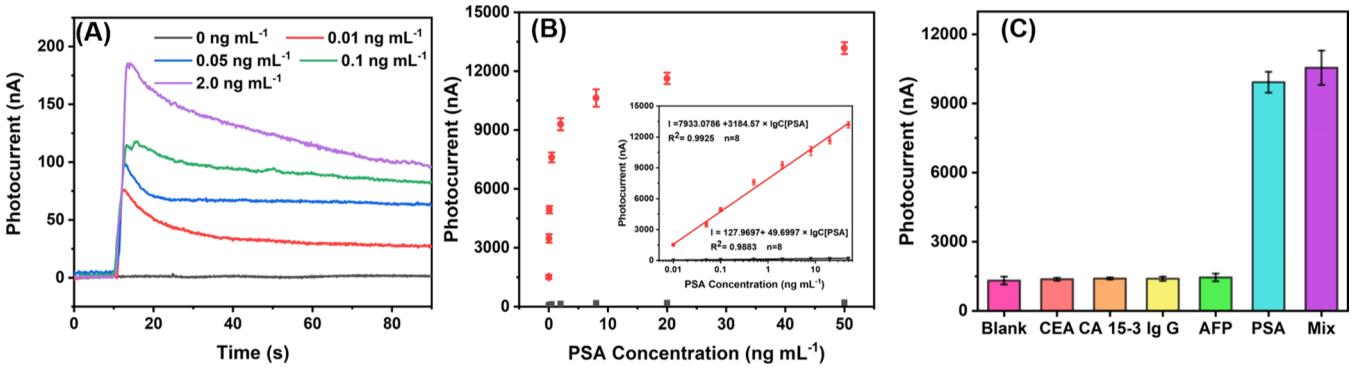

Figure 5. (A) Photocurrent of the PEC-CL platform toward different concentrations of PSA standards (0.01−2.0 ng mL^{-1}); (B) calibration plot of photocurrent response amplified by capacitor *vs* target PSA (inset: linear calibration plot without the capacitor for PSA determination); and (C) selectivity of the PEC-CL biosensor for PSA (4.0 ng mL^{-1}), CEA (80 ng mL^{-1}), CA 15−3 (80 U mL^{-1}), IgG (80 ng mL^{-1}), and AFP (80 ng mL^{-1}) (note: The mixture consisted of all the above interferences together).

functionalized AuNP had a significant absorption around 522 nm, which was similar to previous study, indicating the successful synthesis of ABEI-AuNP composite nanoparticles.[48] To obtain a stable signal output, we structured an autoinjection device model for CL detection. The evaluation of the chemiluminescence stability of the flow injection model was performed by time scan in the phosphor mode of the fluorescence spectrophotometer (FL, F7000, Hitachi), which was mainly used to prevent the generation of fluorescence from ABEI-AuNPs. To further confirm the successful coupling of ABEI on AuNPs, we characterized and proved their catalytic and luminescent properties. As shown in Figure S5, after adding 10 mM hydrogen peroxide, a strong and stable blue light source could be emitted, which proved that ABEI was successfully coupled on AuNPs. As shown in Figure 3C, the ABEI-AuNPs-PIP chemiluminescence system was capable of continuous luminescence for 100 s, with little change in luminescence intensity during flow injection, compared to the direct addition method. The stable and efficient chemiluminescence can meet the satisfactory signal output during PEC measurement.

Characterization of Paper-Based Supercapacitors. Since low photocurrents, caused by weak light intensity, are difficult to display accurately on the DMM, it is necessary to integrate capacitors with charge storage capabilities throughout the PEC test platform. To investigate the performance of the paper supercapacitor for collecting photoelectric signals excited by an external light source, the surface morphology and charge−discharge performance of the capacitors were characterized. The structure and fabrication process of the paper supercapacitor are demonstrated in Figure 4A. Detailed procedures for constructing paper-based capacitors can be found in the Supporting Information. Briefly, the acid-treated carbon paper and the filter paper were adhered to each other by PVA-H_2SO_4, and the all-solid paper supercapacitor was obtained by applying pressure and hot air drying. The upper and lower part of the capacitor were bonded with a current collector (Ag glue) so that the current generated by the PEC process was collected to charge the capacitor and the reverse process thereof. The SEM images of carbon paper with different magnifications are presented in Figure 4B,C. SEM images showed that the graphite paper had a broken sheet structure from the original continuous and uniform layered structure (Figure S6) after acid treatment, which would improve the performance of capacitors.[49] The experimental characterization of the galvanostatic (0.1 mA) charge and discharge of the paper-based supercapacitor is shown in Figure 4D. The areal capacitance value was calculated by the following equation: $C = I\Delta t/A\Delta V$ (note: I is the current applied, A represents the actual area of the capacitor, and ΔV represents the voltage window). Combined with the constant current charge−discharge curve in Figure 4D, it could be calculated that the area capacitance of the PE made was 2.875 μF cm^{-2} at 0.1 mA. Noticeably, there was no significant change in capacitance value during multiple charging and discharging, indicating that the capacitor could be reused at high performance. To further determine the stability of the supercapacitor, 100 cycle charging experiments were performed on the supercapacitor, with the charging time as a standard, and the final results are shown in Figure 4E. No appreciable changes were observed during the 100 cycles of charge and discharge of the capacitor, indicating that the capacitor was robust and fully capable of supporting the current in the photochemical process.

Dose Response of the PEC-CL Platform toward Target PSA. Standard quantitative assays for PSA targets were performed on the PEC-CL platform by optimizing the experimental conditions (shown in the Supporting Information). The photocurrent was recorded on a paper-based photodetector wetted with 0.1 M Na_2SO_4 solution without bias voltage. Figure 5A represents the photocurrent curves toward different concentrations of target PSA, which gradually increased with the increment of target levels, which was attributed to the increase of the light intensity of the chemiluminescent system of ABEI-AuNPs-PIP. A good linear relationship was found between the photocurrent stabilized at a certain value and the target PSA concentration, which could be fitted in the range of 0.01 to 50 ng mL^{-1} (Figure 5B; square plots). Thanks to the persistence and robustness of the flow-injected chemiluminescence, the generated photocurrent could be continuously detected, so that the capacitor would be charged by a photoelectric electrode, followed by an instantaneous amplified current readout using a handheld DMM. The dot plots in Figure 5B represent the relationship between the amplification of the paper capacitor with DMM readout and target PSA. The detection range, regression equation, and limit of detection values (defined the concentration of the target corresponding to a signal-to-noise ratio of 3) were 0.01−50 ng mL^{-1}, I (nA) = 3184.57 × log $C_{[PSA]}$ + 7933.08 (ng mL^{-1}, R^2 = 0.9925, n = 8), and 6.25 pg

https://doi.org/10.1021/acs.analchem.1c03344
Anal. Chem. 2021, 93, 13389−13397

mL^{-1}, respectively. Compared with the PSA detection scheme without capacitor amplification, the method of instantaneous release detection after storing current through the supercapacitor could effectively improve the sensitivity of the target PSA (~64.1 fold). Due to the photochromic nature of TiO_2-g-C_3N_4-PMA, the color change of paper-based electrode during the test (from light white or yellow to blue) simultaneously indicated the PSA concentration. The changes in the photosensitive material on the paper during the PEC process are depicted in the Supporting Information (Scheme S1). Briefly, when a sufficiently energetic light source was used to excite the separation of electrons and holes in the TiO_2-g-C_3N_4 heterojunction, the outer clad PMA acted as an electron acceptor undergoing its own Mo(VI) to Mo(V) reduction, showing that the macroscopic range exhibited a change from yellow to heteropolymeric blue. The transfer path of electrons followed a direct Z-scheme heterojunction, which facilitated the tuning of the band gap of TiO_2 and the efficiency of utilization of visible light.[33,50] Under optimum conditions, the color of the paper-based electrode became darker blue with increasing PSA concentration and could be used as a roughly semiquantitative measurement from 0.1 to 20 ng mL^{-1} (detailed in Figure S7). In addition, the PEC-CL testing platform was comparable to commercially available PSA ELISA kits in terms of detection line and detection range, such as 0.1 ng mL^{-1} for Sangon Biotech (cat#: D721133); 8.0 pg mL^{-1} for Abcam (cat#: ab264615); and 94 pg mL^{-1} for Finetest (cat#: EM1314). Most specifically, the PEC sensor constructed in this paper can meet the requirement of rapid and cost-controlled measurement. Compared with the above-mentioned commercially available PSA Elisa kits, which cost about $10.4 and are cumbersome, the PSA-CL platform constructed in this paper costs about <$1.0 for a single test, which is more favorable for the dissemination in home environments and POCTs in developing countries (The specific cost calculation method is detailed in the Supporting Information).

The specificity and selectivity of the PEC-CL test platform was evaluated by capacitor amplification of photocurrent and background signal, mainly by testing some non-target analytes including carcinoembryonic antigen (CEA), carcinoembryonic antigen (CA 125), immunoglobulin G (Ig G), carcinoembryonic antigen 15−3 (CA 15−3), and alpha-fetoprotein (AFP). The PSA concentration in the test was set at 4.0 ng mL^{-1}, which is commonly used as an indicator of the likelihood of having prostate cancer, and the concentration of the interferents was set to 20 times the PSA concentration (80 ng mL^{-1} or 80 U mL^{-1}). As shown in Figure 5C, all non-target interferents exhibited signals close to the background in the photocurrent test, and in addition, the photocurrent values obtained in the presence of both interferents and target PSA were almost indistinguishable from those in the absence of interferents. The above results indicated that the CL-based PEC sensing platform could be used for the specific detection of PSA.

The accuracy of the PEC-CL sensing platform relative to the PSA ELISA kit was investigated by testing clinical serum specimens in order to meet the testing needs in real-world medical testing settings and home environments. The samples were obtained from the local hospital of our university, and the results of the PEC-CL platform test and PSA ELISA kit test are shown in Table S1. Prior to measurement, these serum specimens were centrifuged for 10 min at 6000*g* at room temperature to remove the possible precipitate. Thereafter, the obtained supernatant was determined with these two methods. The results showed that the CL-PEC sensor could accurately indicate the PSA content in a complex sample and was acceptable compared with the test result of a commercial PSA ELISA kit. The t_{exp} values of all the real samples tested were less than 2.78. The recovery experiments on real samples further demonstrated the good stability and accuracy of the sensing platform with spiked recoveries in the range of 92.2−105.6%. The above results indicated that the PEC sensing platform by coupling with the ABEI-AuNPs-PIP chemiluminescence system can be used for the determination of target PSA in complex biological systems.

CONCLUSIONS

In summary, a multifunctional PEC immunoassay platform with self-powered continuous injection of chemiluminescence was successfully constructed for the sensitive and specific detection of PSAs. The TiO_2-g-C_3N_4-PMA loaded on the PE underwent electron−hole separation and photoreduction of PMA under the excitation of external light, which effectively indicated the PSA content. The advantages of this work are highlighted as follows: (i) self-energized continuous feed ABEI-AuNPs-PIP chemiluminescence system replaces conventional light sources for electron and hole separation in excitation of photoelectronic materials; (ii) the construction of simple and cost-controllable paper-based photoelectrodes and PEC sensing platforms facilitates the promotion of point-of-care detection in countries that are lagging behind in development; and (iii) TiO_2-g-C_3N_4 Z-scheme heterojunction based on PMA is synthesized, which is used for multisignal output in the PEC biological detection process. This is a key study that holds great promise for future clinical testing and promotion and testing in low development areas by building a PEC biosensing platform that is low cost, simple to operate, has good user interaction, and is integrated with portability and sensitivity.

ASSOCIATED CONTENT

Supporting Information

The Supporting Information is available free of charge at https://pubs.acs.org/doi/10.1021/acs.analchem.1c03344.

Chemical and reagent, preparation of mAb_1-MB and ABEI-AuNPs-pAb_2 probe, fabrication of paper-based sandwich capacitor, optimization of experimental conditions, zeta potentials of nanomaterial, TEM and EDS of TiO_2-based nanocomposite, ATR spectra of g-C_3N_4, XPS analysis of the Ti element, luminescence diagram of H_2O_2 catalyzed by Au-ABEI, SEM images of the graphite paper, chromatogram of PE, result of optimization of experimental conditions, photoexcitation and photoreduction processes, and comparison of the assayed results (PDF)

AUTHOR INFORMATION

Corresponding Author

Dianping Tang − *Key Laboratory of Analytical Science for Food Safety and Biology (MOE & Fujian Province), Department of Chemistry, Fuzhou University, Fuzhou 350108, People's Republic of China; Chongqing Vocational Institute of Engineering, Chongqing 402260, People's Republic of China;* orcid.org/0000-0002-0134-3983;

https://doi.org/10.1021/acs.analchem.1c03344
Anal. Chem. 2021, 93, 13389−13397

Phone: +86-591-2286 6125; Email: dianping.tang@fzu.edu.cn; Fax: +86-591-2286 6135

Authors

Zhichao Yu − *Key Laboratory of Analytical Science for Food Safety and Biology (MOE & Fujian Province), Department of Chemistry, Fuzhou University, Fuzhou 350108, People's Republic of China*

Hexiang Gong − *Key Laboratory of Analytical Science for Food Safety and Biology (MOE & Fujian Province), Department of Chemistry, Fuzhou University, Fuzhou 350108, People's Republic of China*

Yuxuan Li − *Key Laboratory of Analytical Science for Food Safety and Biology (MOE & Fujian Province), Department of Chemistry, Fuzhou University, Fuzhou 350108, People's Republic of China*

Jianhui Xu − *Key Laboratory of Analytical Science for Food Safety and Biology (MOE & Fujian Province), Department of Chemistry, Fuzhou University, Fuzhou 350108, People's Republic of China*

Jin Zhang − *Chongqing Vocational Institute of Engineering, Chongqing 402260, People's Republic of China*

Yongyi Zeng − *The United Innovation of Mengchao Hepatobiliary Technology Key Laboratory of Fujian Province, Mengchao Hepatobiliary Hospital of Fujian Medical University, Fuzhou 350025, People's Republic of China*

Xiaolong Liu − *The United Innovation of Mengchao Hepatobiliary Technology Key Laboratory of Fujian Province, Mengchao Hepatobiliary Hospital of Fujian Medical University, Fuzhou 350025, People's Republic of China;* orcid.org/0000-0002-3096-4981

Complete contact information is available at: https://pubs.acs.org/10.1021/acs.analchem.1c03344

Notes

The authors declare no competing financial interest.

■ ACKNOWLEDGMENTS

We gratefully acknowledge the financial support from the National Natural Science Foundation of China (grant nos. 21874022 and 21675029) and the Natural Science Foundation of Chongqing (grant no. cstc2020jcyj-msxmX0977).

■ REFERENCES

(1) Ming, T.; Luo, J.; Liu, J.; Sun, S.; Xing, Y.; Wang, H.; Xiao, G.; Deng, Y.; Cheng, Y.; Yang, Z.; Jin, H.; Cai, X. *Biosens. Bioelectron.* **2020**, *170*, 112649.
(2) Zhu, G.; Yin, X.; Jin, D.; Zhang, B.; Gu, Y.; An, Y. *TrAC, Trends Anal. Chem.* **2019**, *111*, 100−117.
(3) Nilghaz, A.; Guan, L.; Tan, W.; Shen, W. *ACS Sens.* **2016**, *1*, 1382−1393.
(4) Yao, B.; Zhang, J.; Kou, T.; Song, Y.; Liu, T.; Li, Y. *Adv. Sci.* **2017**, *4*, 1700107.
(5) Li, S.-X.; Xu, X.-L.; Yang, Y.; Xu, Y.-S.; Xu, Y.; Xia, H. *ACS Appl. Mater. Interfaces* **2021**, *13*, 31919−31927.
(6) Sala de Medeiros, M.; Chanci, D.; Martinez, R. V. *Nano Energy* **2020**, *78*, 105301.
(7) Sun, J.; Li, L.; Ge, S.; Zhao, P.; Zhu, P.; Wang, M.; Yu, J. *ACS Appl. Mater. Interfaces* **2021**, *13*, 3645−3652.
(8) Li, L.; Zhang, Y.; Yan, Z.; Chen, M.; Zhang, L.; Zhao, P.; Yu, J. *ACS Sens.* **2020**, *5*, 1482−1490.
(9) Brazaca, L. C.; Moreto, J. R.; Martín, A.; Tehrani, F.; Wang, J.; Zucolotto, V. *ACS Nano* **2019**, *13*, 13325−13332.
(10) Komatsu, T.; Maeki, M.; Ishida, A.; Tani, H.; Tokeshi, M. *ACS Sens.* **2020**, *5*, 1287−1294.
(11) Ninwong, B.; Ratnarathorn, N.; Henry, C. S.; Mace, C. R.; Dungchai, W. *ACS Sens.* **2020**, *5*, 3999−4008.
(12) de Araujo, W. R.; Frasson, C. M. R.; Ameku, W. A.; Silva, J. R.; Angnes, L.; Paixão, T. R. L. C. *Angew. Chem.* **2017**, *56*, 15113−15117.
(13) Wang, Y.; Luo, J.; Liu, J.; Li, X.; Kong, Z.; Jin, H.; Cai, X. *Biosens. Bioelectron.* **2018**, *107*, 47−53.
(14) Yu, H.; Tan, X.; Sun, S.; Zhang, L.; Gao, C.; Ge, S. *Biosens. Bioelectron.* **2021**, *185*, 113250.
(15) Wang, Y.; Zhang, L.; Kong, Q.; Ge, S.; Yu, J. *Biosens. Bioelectron.* **2018**, *120*, 64−70.
(16) Montali, L.; Calabretta, M. M.; Lopreside, A.; D'Elia, M.; Guardigli, M.; Michelini, E. *Biosens. Bioelectron.* **2020**, *162*, 112232.
(17) Vizzini, P.; Manzano, M.; Farre, C.; Meylheuc, T.; Chaix, C.; Ramarao, N.; Vidic, J. *Biosens. Bioelectron.* **2021**, *171*, 112689.
(18) Liu, C.-C.; Wang, Y.-N.; Fu, L.-M.; Huang, Y.-H. *Chem. Eng. J.* **2018**, *332*, 695−701.
(19) Luo, Z.; Lv, T.; Zhu, K.; Li, Y.; Wang, L.; Gooding, J. J.; Liu, G.; Liu, B. *Angew. Chem., Int. Ed.* **2020**, *59*, 3131−3136.
(20) Gao, Z.; Qiu, S.; Yan, F.; Zhang, S.; Wang, F.; Tian, W. *Chem. Sci.* **2021**, *12*, 10041−10047.
(21) Zhao, W.-W.; Xu, J.-J.; Chen, H.-Y. *Chem. Soc. Rev.* **2015**, *44*, 729−741.
(22) Shu, J.; Tang, D. *Anal. Chem.* **2020**, *92*, 363−377.
(23) Zhou, Q.; Tang, D. *TrAC, Trends Anal. Chem.* **2020**, *124*, 115814.
(24) Zhao, W.-W.; Xu, J.-J.; Chen, H.-Y. *Biosens. Bioelectron.* **2017**, *92*, 294−304.
(25) Shu, J.; Qiu, Z.; Zhou, Q.; Lin, Y.; Lu, M.; Tang, D. *Anal. Chem.* **2016**, *88*, 2958−2966.
(26) Dong, Y.-X.; Cao, J.-T.; Wang, B.; Ma, S.-H.; Liu, Y.-M. *ACS Appl. Mater. Interfaces* **2018**, *10*, 3723−3731.
(27) Ge, S.; Liang, L.; Lan, F.; Zhang, Y.; Wang, Y.; Yan, M.; Yu, J. *Sens. Actuators, B* **2016**, *234*, 324−331.
(28) Shen, S.; Chen, J.; Wang, M.; Sheng, X.; Chen, X.; Feng, X.; Mao, S. S. *Prog. Mater. Sci.* **2018**, *98*, 299−385.
(29) Gao, B.; Zhao, X.; Liang, Z.; Wu, Z.; Wang, W.; Han, D.; Niu, L. *Anal. Chem.* **2021**, *93*, 820−827.
(30) Khan, S.; Lemes Ruwer, T.; Khan, N.; Köche, A.; Lodge, R. W.; Coelho-Júnior, H.; Sommer, R. L.; Leite Santos, M. J.; Malfatti, C. F.; Bergmann, C. P.; Fernandes, J. A. *J. Mater. Chem. A* **2021**, *9*, 12214−12224.
(31) Qiu, Z.; Shu, J.; Tang, D. *Anal. Chem.* **2018**, *90*, 1021−1028.
(32) Si, R.; Xie, X.; Li, T.; Zheng, J.; Cheng, C.; Huang, S.; Wang, C. *ACS Sens.* **2020**, *5*, 1345−1353.
(33) Li, Y.; Lv, K.; Ho, W.; Dong, F.; Wu, X.; Xia, Y. *Appl. Catal., B* **2017**, *202*, 611−619.
(34) Horn, M. R.; Singh, A.; Alomari, S.; Goberna-Ferrón, S.; Benages-Vilau, R.; Chodankar, N.; Motta, N.; Ostrikov, K.; MacLeod, J.; Sonar, P.; Gomez-Romero, P.; Dubal, D. *Environ. Sci. Technol.* **2021**, *14*, 1652−1700.
(35) Liu, R.; Streb, C. *Adv. Energy Mater.* **2021**, *11*, 2101120.
(36) Jia, X.; Shen, L.; Yao, M.; Liu, Y.; Yu, W.; Guo, W.; Ruan, S. *ACS Appl. Mater. Interfaces* **2015**, *7*, 5367−5372.
(37) Zou, Y.-G.; Meng, F.; Xiao, D.; Sheng, H.; Chen, W.-P.; Meng, X.-H.; Du, Y.-H.; Gu, L.; Shi, J.-L.; Guo, Y.-G. *Nano Energy* **2021**, *87*, 106172.
(38) Taghavi, M.; Tabatabaee, M.; Ehrampoush, M. H.; Ghaneian, M. T.; Afsharnia, M.; Alami, A.; Mardaneh, J. *J. Mol. Liq.* **2018**, *249*, 546−553.
(39) Zhang, B.; Asakura, H.; Zhang, J.; Zhang, J.; De, S.; Yan, N. *Angew. Chem.* **2016**, *55*, 8319−8323.
(40) Zhang, X.-m.; Zhang, Z.; Zhang, B.; Yang, X.; Chang, X.; Zhou, Z.; Wang, D.-H.; Zhang, M.-H.; Bu, X.-H. *Appl. Catal., B* **2019**, *256*, 117804.
(41) Yang, S.; Zhao, J.; Tricard, S.; Yu, L.; Fang, J. *Anal. Chim. Acta* **2020**, *1094*, 80−89.

(42) Gao, J.; Yang, T.; Wang, X.; He, Q.; He, P.; Jia, L.; Du, L.; Deng, H.; Zhang, H.; Jia, B.; He, X.; Tang, B. *Microchem. J.* **2020**, *158*, 105158.
(43) Jeber, J. N.; Hassan, R. F.; Hammood, M. K.; Al-Jeilawi, O. H. R. *Sens. Actuators, B* **2021**, *341*, 130009.
(44) Zou, W.; González, A.; Jampaiah, D.; Ramanathan, R.; Taha, M.; Walia, S.; Sriram, S.; Bhaskaran, M.; Dominguez-Vera, J. M.; Bansal, V. *Nat. Commun.* **2018**, *9*, 3743.
(45) Wang, H.; Yuan, X.; Wang, H.; Chen, X.; Wu, Z.; Jiang, L.; Xiong, W.; Zeng, G. *Appl. Catal., B* **2016**, *193*, 36−46.
(46) Wei, Y.; Han, B.; Dong, Z.; Feng, W. *J. Mater. Sci. Technol.* **2019**, *35*, 1951−1958.
(47) Wang, Y.; Wang, Y.; Kang, W.; Cao, D.; Li, C.; Cao, D.; Kang, Z.; Sun, D.; Wang, R.; Cao, Y. *Adv. Sci.* **2019**, *6*, 1801222.
(48) Tian, D.; Zhang, H.; Chai, Y.; Cui, H. *Chem. Commun.* **2011**, *47*, 4959−4961.
(49) Zheng, Y.; Zhao, W.; Jia, D.; Liu, Y.; Cui, L.; Wei, D.; Zheng, R.; Liu, J. *Chem. Eng. J.* **2020**, *387*, 124161.
(50) Xu, Q.; Zhang, L.; Yu, J.; Wageh, S.; Al-Ghamdi, A. A.; Jaroniec, M. *Mater. Today* **2018**, *21*, 1042−1063.

https://doi.org/10.1021/acs.analchem.1c03344
Anal. Chem. 2021, 93, 13389−13397